Fabrication and Characterisation of Short Fibre Reinforced Elastomer Composites for Bending and Twisting Magnetic Actuation

David C. Stanier[a], Jacopo Ciambella[b,a], Sameer S. Rahatekar[a]

[a] *Advanced Composites Centre for Innovation and Science, University of Bristol, BS8 1TR, Bristol, UK*

[b] *Dipartimento di Ingegneria Strutturale e Geotecnica, Sapienza Università di Roma, 00184, Rome, Italy*

Abstract

Polydimethylsiloxane (PDMS) films reinforced with short Nickel-coated Carbon Fibres (NiCF) were successfully fabricated, with the fibres aligned along different directions using an external magnetic field. The fibres were dispersed in the host matrix using sonication and mechanical mixing before being cured for 48 hours in the magnetic field; thanks to the nickel functionalisation, the fibre orientation was achieved by a low intensity field (< 0.2 T) which required an inexpensive experimental set-up. The main focus of this study was looking at the actuation potential of this magnetic composite material; successful actuation was achieved, showing its large displacement capability. The results confirm the presence of an instability controlled by the magnetic torque, as predicted by the introduced model. The composite films undergo a transition from a bending-only deformed configuration for the 0° fibre specimen, to a twisting-only configuration, achieved for fibres at 90°, whereas all the intermediate angles show both bending and twisting. This behaviour mirrors that which is used to propel a selection of marine mammals.

Keywords: Fibre Alignment, Anisotropy, Magnetic Torque, Instability

Email addresses: david.stanier@bristol.ac.uk (David C. Stanier), jacopo.ciambella@uniroma1.it (Jacopo Ciambella), sameer.rahatekar@bristol.ac.uk (Sameer S. Rahatekar)

1. Introduction

To enhance the mechanical properties of elastomer materials, reinforcements are often used. The use of discontinuous fibres is often motivated by the increased surface area and therefore the increased surface interaction with the matrix, when compared to spherical inclusions (such as Carbon black). However, they are usually randomly dispersed to give an overall isotropic behaviour, except in those cases when the manufacturing process imparts some anisotropy (e.g. extrusion).

The advantages and challenges in controlled orientation of materials in solution have been studied [29], and have included various manufacturing methods, for example, shear [33], electrical [23] and magnetic alignment [28, 2, 7]; the latter of which has demonstrated controlled 3-dimensional reinforcement [7] and the complex arrangement of reinforcements into assemblies for optimal smart elastomer material properties [24]. The industrial potential of such a material is known [5], and as such significant research has been employed to understand the factors underpinning the orientation of magnetic fibres in a solution, such as field strength [18], field direction [7], and particle morphology [7], in order to spatially control the reinforcements. This could increase the mechanical properties, but can also add a degree of multi-functionality. For instance, the aligned fibres can also provide control of other material properties such as the electrical conductivity [15, 23], dielectric [32], energy dissipation [2], gas permeability [32] and thermal conductivity [3].

Erb et al. [7] have researched the effects of particle size and magnetic field strength on the alignment of Ultra High Magnetic Response (UHMR) particles in the host matrix. Particles in the size range of 10 μm give the optimum response, as these only require a very low magnetic field, less than 2 mT, in order to align them effectively in the host matrix. On the contrary, particles on the nanoscale and particles greater than a few micrometres require a higher magnetic torque to align them. This is due to the thermal forces dominating at smaller scales and gravitational forces dominating for much larger particles. This has been observed for nanoparticles by Takeyama et al. [35], showing that a pulsed magnetic field strength in the region of 40 T was required to obtain good alignment of single wall carbon nanotubes in a sodium dodecyl sulphate surfactant. Further studies corroborate this data showing that a magnetic field in excess of 10 T can achieve good alignment at room temperature, and as the magnetic field strength increases the alignment becomes more effective [29, 7]. In References [38, 39] uniform magnetic

fields with low intensity (< 100 mT) were used to align spherical Fe_3O_4 particles into a PDMS matrix: due to particle-particle interactions, which become dominant when the particles are closely spaced, a pearl chain structure was achieved, where all the particles were aligned along the magnetic field direction, making the resulting material strongly anisotropic.

It is also possible to utilize the reinforcement and material properties to actuate a specimen of the material, for example the magnetic torque on magnetically responsive reinforcements is transferred to the matrix and can cause locomotion and deformation of the specimen. This effect can be instantaneous/in-line with the field properties [38], or can be coupled to smart memory effects [27] and bi-stabilities [11], to 'lock' the configurational changes. The use of external stimuli in controlling the actuation of materials is determined by the relationship between the mechanical and field responsiveness. This has led to a number of theoretical and numerical models to describe the relationship and the subsequent material behaviour in a magnetic/electric field [1, 9, 22, 30, 31], as well as the resulting breakdown of these relationships in smart materials, due to mechanical testing [36], **or the instabilities that arise as a result of the coupling between multifunctional properties [19]**.

An understanding of these effects can lead to the creation of a number of interesting actuation effects [8, 37]. **And in fact, the high responsiveness, large strain capabilities and viscoelastic behaviour of elastomers [34] mean they are ideal materials for such responsive devices [21, 20]**. Kimura et al. [16] produced a carbon fibre/agarose gel composite in which carbon fibres were radially embedded in the gel; by subjecting the sample to a strong homogeneous magnetic field (up to 8 T), large deformations were observed. A similar technique was applied in [17] to produce a silicon rubber-steel wire composite which was actuated with much lower field intensities (≈ 0.2 T). Zrìnyi and coworkers [40] produced a hydrogel filled with spherical magnetic particles (Fe_3O_4) and embedded it into a non-homogeneous field. By controlling the intensity of the field, they were able to trigger non-continuous shape changes (instabilities) which are caused by the forces acting on the spherical particles and produced by the non-homogeneous field; the same effect couldn't be triggered by a uniform field due to the absence of magnetic forces.

The key advantage of aligning magnetic reinforcements, and using that induced magnetic responsiveness of the material, is that the actuation direction is controlled, both by the non-isotropic mechanical properties and the

non-isotropic magnetic responsiveness. Furthermore, magnetic actuation has the benefit over similar micro-motor systems, such as those that use chemical propulsion, of the magnetic force being contactless and therefore non-invasive when used to propel a system for bio-medical applications.

This study looks at the creation of a novel polydimethylsiloxane (PDMS) composite reinforced with Nickel-coated Carbon Fibres (NiC) which could potentially lead to novel micro-swimmer devices. Development of micro- and nano-scale swimmers has become an area of interest in recent years due to the potential these systems have in transforming drug delivery systems, lab-on-chip devices and also cultivating new methods for performing micro-surgery and nano/micro fabrication [25]. The main focus of research in this area has been based on the development of helical micro-swimmers that are propelled through the water using rotating magnetic fields, these systems show promise due to them having good steering ability and the potential to achieve high propulsion speeds [14]. Biomimicry of aquatic propulsion has also led to the development of electro-active polymers that mimic the actuation surfaces of fish, with controlled bending and twisting configurations achievable and determined by the placement of electrodes on the surfaces [12]. Other systems use alternative propulsion techniques such as chemical reactions, bubble oscillation and bacteria mimicry [13]. Although these devices all show promise, there are still difficulties in developing swimmers that are easy to fabricate and reproduce, as well as being bio-compatible for use in the bio-medical field.

In this study, rectangular PDMS specimens with different fibre alignment angles were produced and tested to evaluate the influence of the fibre orientation upon the mechanical and magnetic properties. The particles being used were Carbon Fibres in the region of 250 μm coated with Nickel, that thanks to this ferromagnetic coating, require low field intensities to be oriented and actuated. The carbon fibres, Nickel and PDMS are all bio-compatible and are therefore ideal for use in bio-medical applications [6]. The dispersion and distribution methods are presented, showing how it was possible to tailor the directional properties of the material and therefore obtain varying actuation properties depending on the fibre orientation. Aligning the particles in the host matrix enhances the materials capability to deform when in the presence of an externally applied magnetic field. The magnetic torques responsible for the alignment of the fibres are further used to trigger abrupt shape changes in the material which actually correspond to a shift in the equilibrium states of the system. Results of static testing are presented to

give a detailed understanding of the material actuation properties.

2. Sample Preparation

To create the magnetically actuated elastomer samples, the matrix of PDMS was reinforced with NiC fibres with length $\sim$250 μm and diameter 4.8 μm (aspect ratio $\sim$52, Ni 40 wt%). The dimensions of the fibres were chosen for optical observation of the alignment, in-situ and post-cure, whilst considering the difficulty to orient longer fibres in viscous solutions. The fibres were added to the base component of SYLGARD 184 in a ratio of 10:1 and mechanically mixed for 5 minutes. To achieve good dispersion of these particles in the host matrix the solution was immersed in an ultra-sonication bath for 50 minutes and then mechanically mixed for a further 5 minutes. Sonication was then performed for a final 50 minutes before leaving the solution to rest for 12 hours. After the solution had settled, the top 90% was separated leaving the lower 10% that contained a higher density of the NiC fibres. These fibres were either heavier or did not adhere as well to the host matrix and therefore dropped to the bottom of the mixture. By removing this small fraction of the PDMS-NiC solution the final mixture contained the fibres that achieved better matrix-particle interaction.

The required hardener was then added to the PDMS-NiC solution at a ratio of 10:1 and mechanically mixed for 5 minutes. This mixture was added to a cast of size 26 mm by 34 mm and placed in a magnetic field to align the fibres in the required directions, creating transversely isotropic samples. The solution was then left to set for 48 hours at room temperature to ensure the fibres were aligned effectively in the host matrix. The permanent magnets and apparatus used to align the fibres are shown in Fig. 1. Preliminary tests were performed on the magnetic arrangement to ensure the homogeneity of the fibres post-cure, and that orientation of the fibres has occurred. The homogeneity of the magnetic field is of importance so that the fibres orient themselves parallel to the magnetic field due to the magnetic torque; if the magnetic field was non-homogeneous then the fibres would also translate and hence agglomerate close to the boundary of the petri dish. As such the resulting material would be non-homogeneous.

Once cured, the specimens were cut from the petri dish at predefined fibre orientation angles between 0° and 90° degrees, 2 specimens cut from each petri dish with a dumbbell cutting tool (Fig. 2). A total of 6 specimens were made at each fibre angle θ_0 =[0, 15, 30, 45, 60, 75, 90]. A concentration

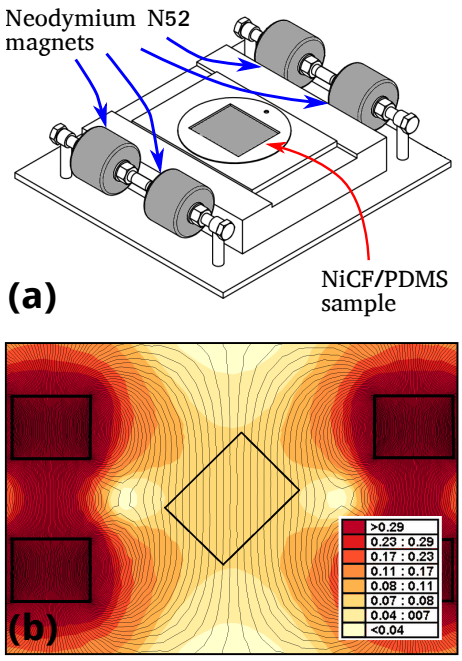

Figure 1: (a) Magnetic setup for specimen curing. The specimen is suspended in the centre of four Neodymium N52 magnets to produce a homogeneous magnetic field. (b) The magnetic field intensity calculated in the FE environment FEMM [26] for a specimen at 45°. Note that the specimen is much thinner than the radius of the magnets, meaning the change in magnetic field through the thickness is negligible as confirmed by the even fibre distribution in the specimen cross-section observed by optical microscopy.

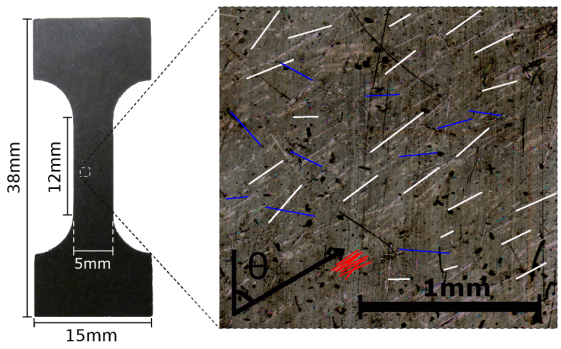

Figure 2: Dumbbell test coupon and inset micrograph of a 60° specimen. Selected fibres highlighted in white; misaligned fibres in blue, and agglomeration of fibres in red (for illustrative purposes only).

of NiC of 6 wt% was calculated post-cure by burn-off of the PDMS mixture. This is likely to be a slight overestimation due to the production of SiO_2 in the presence of oxygen during the degradation of PDMS.

3. Results

3.1. Microscopy/SEM Results

Prior to mechanical testing, an image of each specimen was captured by optical microscopy (Fig. 2). This micrograph of the specimen was post-processed so that a 6 mm x 4 mm section of the specimen was analysed using Image software to create an image layer onto which the fibres are drawn; this layer is then imported to the MATLAB (ver.2012b1) Image Processing Toolbox and information on the fibre position, orientation and size is determined. Fibres that overlap are treated in separate image layers, therefore ensuring agglomerations are not treated as a single fibre. The alignment of the fibres and formation of stable dispersions within the host matrix is necessary to optimise the material properties. Figure 2 shows the particle alignment and dispersion within the PDMS matrix. It is observed from the results that good dispersion was achieved in-plane and through the thickness of the sample (see Fig.8c), although a small number of undesirable agglomerations were present in the final material as shown by the red fibres in Fig. 2.

Figure 3a & b show the typical distribution curves for a specimen, with the majority of the fibres being aligned to the direction of the magnetic field.

Although there is an underlying homogeneous dispersion of fibres that do not orient, which is thought to be caused by the nickel coating being no longer present in these cases.

To confirm these findings, SEM images of the fibres were taken before sonication and curing (Fig. 4). Although the majority of fibres were intact (Fig. 4a), the average fibre length is shorter than reported by the manufacturer due to the many features of geometrical irregularities and damage that can be observed (Fig. 4b - 4f), which justify the presence of fibres which were not aligned by the magnetic field. Some additional damage is also likely to occur during the sonication and mechanical mixing processes, however these effects are expected to be limited.

3.2. Mechanical Testing

All mechanical tests were performed at room temperature, with dumbbell specimens conforming to ASTM standard D1708, and a specimen thickness of approximately 0.6 mm. The engineering stress is determined as the ratio of the measured force to the original specimen cross-sectional area, whilst the strain is the ratio of the extension to the original distance and is calculated by digital image correlation (DIC). Uniaxial mechanical testing was performed using an Instron testing machine. Six specimens at each angle were tested, at a strain rate of 1.36 x $10^{-2}s^{-1}$ in the gauge length, by applying displacement control (10 mm/min) until rupture.

The results of the large strain tensile tests are shown in Fig. 5 for 0°, 30°, 60° and 75°. The differences in the stress-strain curves highlight the different stress transfer mechanisms that take place during deformation and cause the large variation of the tensile modulus at small strain seen in the figure. When the fibres are oriented in the loading direction (such as in the case of the 0° and 30° specimens) they are able to carry the majority of the load and a high modulus is achieved; on the contrary, low moduli correspond to configurations where the fibres are almost orthogonal to the loading.

These results can be effectively interpreted by comparison with the transversally isotropic hyperelastic model used in Ciambella and Stanier [4]. The main underlying hypothesis of the model considers that the strain energy density of the reinforced material is separable into two contributions: one accounting for the overall stretch of the PDMS matrix and the other weighing the stretch along the stiff fibres. For such a model, the expression of the effective tangent modulus (Young's modulus) in the direction of the tensile

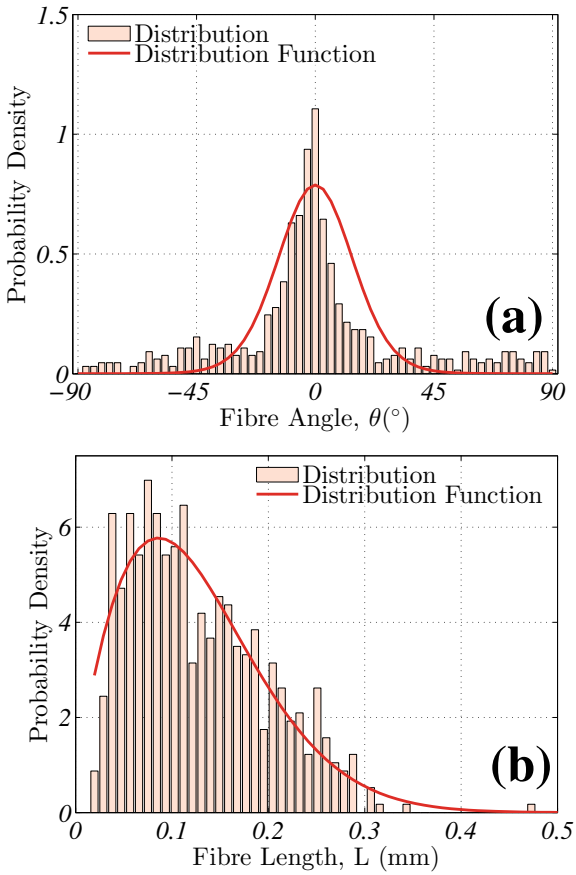

Figure 3: Distributions extracted from a micrograph of a 0° specimen, sampling $\geq$ 600 fibres. (a) Fibre Orientation Distribution (see [18]), $\rho(\theta) = \exp(b\ cos(2\theta))/\left(\int_{-\pi/2}^{\pi/2} \exp(b\ cos(2\theta))d\theta\right)$ (b = 4.49 $\pm$0.57). (b) Fibre Length Distribution, $h(L) = \frac{1}{(\sqrt{2\pi}\ c)} \exp(\frac{-(L-d)^2}{(2c^2)})$ (c = 0.068 $\pm$0.011, d = 0.089 $\pm$0.017). The average parameter values are given for 6 samples, with standard deviations.

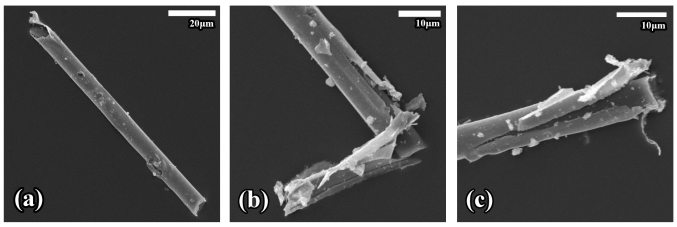

Figure 4: NiC fibres characterisation under SEM. (a) An intact fibre; (b) broken fibre; (c) broken interface.

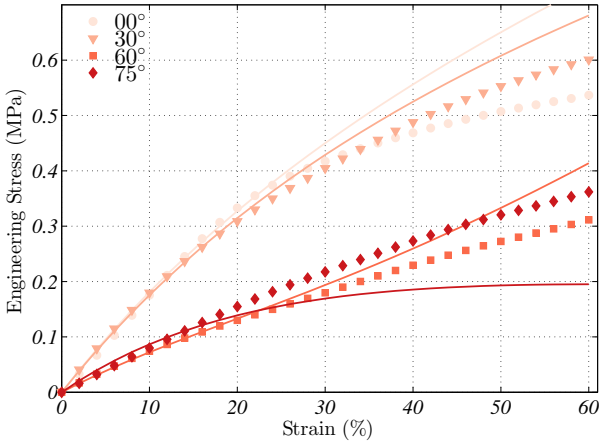

Figure 5: Large strain experimental results (dots) compared to the transversely hyperelastic isotropic constitutive model (continuous lines) in Reference [4] for angles $\{0°, 30°, 60°, 75°\}$.

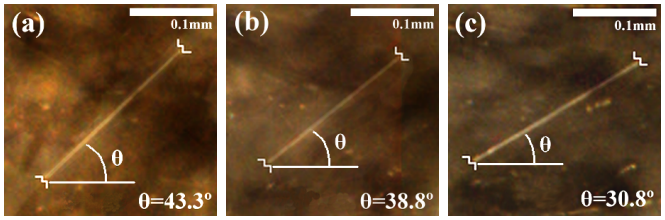

Figure 6: Experimental micrographs of fibre rotation in the PDMS matrix at different strain levels (0% (a), 23% (b) and 55% (c)), for a specimen with initial angle of the fibres at 45°.

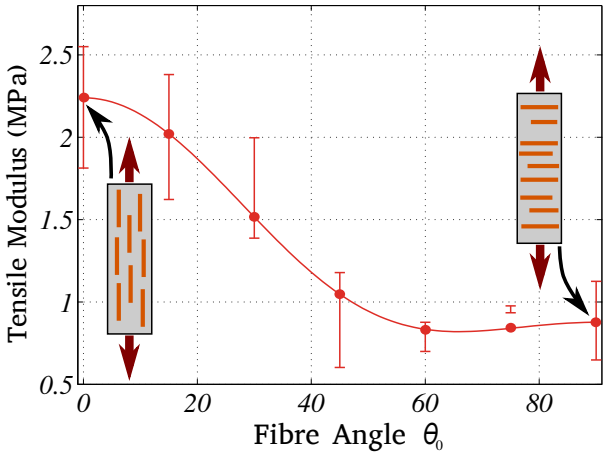

Figure 7: Variation of the tensile modulus at small strain in terms of fibre angle θ_0 fitted to Eq. 1 ($\mu = 1.579{\times}10^{-1}$ MPa, $\alpha = 1.850$, $\beta = 2.878$). Confidence intervals of 90% shown for each angle.

loading is

$$E(\theta_0) = \frac{3\mu}{16}\left[16 + 16\alpha + 5\beta + 8\beta\cos\left(2\theta_0\right) + 3\beta\cos\left(4\theta_0\right)\right], \tag{1}$$

where $\mu \geq 0$, $\alpha \geq -1$, $\beta > 0$ are selected such that the Young's modulus, E, is always positive. Equation 1 is able to describe the dependence of the Young's modulus on the fibre orientation well, as shown by the fitting in Fig. 7. $E(\theta)$ has a minimum for fibres oriented at $\theta_0 = 65.9°$ as corroborated by the stress-strain data in Fig. 5. For this angle, the fibre provides the least amount of resistance to the uniaxial forces imposed upon the specimen. On the contrary for 0° or 90°, the effective modulus has a local maxima (see Fig. 7). The maximum at 0° being significantly larger than at 90°. However, the limiting value at 90° is interesting as it indicates the potential importance of the lateral constraint of the reinforcement in an incompressible system.

At strains above ∼30% the model begins to struggle to capture the behaviour observed in the experimental data in Fig. 5a. In particular, the initial modulus of the 0° specimen in the experimental data is higher, but at 35% of deformation, the rotation of the fibre towards the loading direction causes the 30° specimen tangent modulus to decrease less and the stress to rise above the other. A similar occurrence is not observed between the 60° and 75° specimens and can not be captured by the hyperelastic model. This suggests that the behaviour is likely due to the interfacial effects arisen by

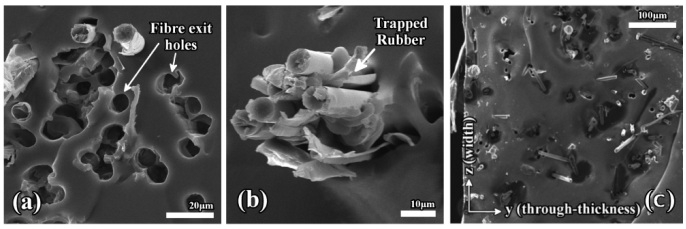

Figure 8: Interface of the fractured PDMS specimens. (a) Poor interface showing fibres pulled out without PDMS attached . (b) Trapped rubber between bundles of fibres. (c) Distribution of the fibres along the through-thickness direction.

the weak matrix/fibre interface and the inclination angle of the reinforcement, that would require further investigation if the device were used at strains larger than $\sim$30%. SEM images of a fractured specimen shown in Fig. 8 corroborate this hypothesis: it is clearly seen that some of the fibres are pulled out from the matrix without any PDMS being attached to them, which suggest a weak bonding between the fibres and the matrix. Although a poor interface worsens the mechanical properties, at large strain it would not be a significant issue for the present micro-swimming application and in fact, the deformations obtained by magnetically actuating a thin specimen are rarely larger than $5 - 10\%$.

The effects of the magnetic field on the stress-strain curves were also investigated and are reported in the supplementary materials. The results showed a negligible effect of the magnetic field on the tensile modulus due to the low fibre content. Similar results have been reported in the open literature [39, 17].

3.3. Actuation Results

The actuation capabilities of the material are driven by the external magnetic field, and the final shape is determined by the balance of magnetic and elastic energies. Several samples with different fibre orientations were tested by cutting a rectangular shaped specimen and vertically suspending it between the plates of an electromagnet in the cantilever configuration sketched in Fig. 9. The magnetic field produced is homogeneous, orthogonal to the fibres and its intensity can be controlled by varying the current absorbed by the electromagnet. When the fibres and the magnetic field are orthogonal no torque acts on the sample and it remains undeformed until the magnetic field reaches a critical value at which the configuration becomes unstable.

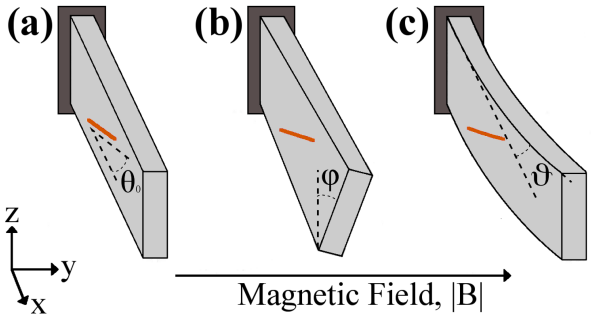

Figure 9: Schematic representation of the actuator model. (a) The undeformed configuration showing the reinforcement angle in the x-z plane, θ_0. (b) The twisting angle, φ. (c) The bending angle, ϑ.

The main advantage of this configuration consists in having different actuator responses based on the initial fibre angle θ_0. The actuation angle is determined by incrementally increasing the magnetic field, and taking a high resolution photograph of the stable specimen position at each magnetic field intensity. The images are then cross-correlated with respect to the initial undeformed configuration.

To investigate this behaviour we introduce a large rotations beam model for which the total energy is the sum of an elastic and a magnetic part, i.e.,

$$E_{tot}(\theta_0, \vartheta, \varphi) = h\, t \int_0^L (\Psi_e + \Psi_m)\, \mathrm{d}s \tag{2}$$

where θ_0 is the angle of the fibres in the undeformed configuration, and $\vartheta = \vartheta(s)$ and $\varphi = \varphi(s)$ the bending and twisting angles of the beam section at abscissa s ($0 \leq s \leq L$) (see Fig. 9); h, t and L are the beam width, thickness and length, respectively. Note that in writing down the integral in (2) over the beam volume rather than the entire space, we have implicitly assumed that the effects of the fibre magnetisation on the external field are negligible.

A suitable model for the elastic Ψ_e and magnetic Ψ_m free energy densities is

$$\Psi_e = \frac{\mathrm{EI}}{2\,L^2}\,\vartheta'(s)^2 + \frac{\mathrm{GJ}}{2\,L^2}\,\varphi'(s)^2\,, \qquad \Psi_m = -\frac{\chi}{2}(\boldsymbol{n}.\boldsymbol{B})^2\,, \tag{3}$$

that could account for large rotations/displacements of the beam. In (3), $\boldsymbol{B}$ is the magnetic field induction and $\boldsymbol{n}$ the orientation of the fibre in the

deformed configuration; as such it can be expressed in terms of the mechanical descriptors ϑ and φ, i.e.,

$$n_x = \sin(\theta_0)\sin(\vartheta)\sin(\varphi) + \cos(\theta_0)\cos(\vartheta) \tag{4}$$

$$n_y = \cos(\theta_0)\sin(\vartheta) - \sin(\theta_0)\cos(\vartheta)\sin(\varphi) \tag{5}$$

$$n_z = \sin(\theta_0)\cos(\varphi)\,. \tag{6}$$

and introduces a coupling between the elastic and the magnetic parts of the energy. By choosing Ψ_m as in (3), we have implicitly assumed the magnetisation of the sample is a linear function of the magnetic field strength B, which is **confirmed by vibrating sample magnetometer (VSM)**.

The other parameters in (3) are $\chi = \chi_a\,\nu_f/(2\mu_0)$ where χ_a represents the magnetic anisotropic susceptibility, μ_0 the vacuum permittivity and ν_f is the volume fraction of the fibres [16]. EI and GJ are the bending and twisting rigidities, respectively.

In order to study the equilibrium shape of the specimen we look for a minimum of the total energy E_{tot} when the bending and twisting angles have the expression:

$$\vartheta(s) = \frac{\vartheta_m}{L}\,s, \qquad \varphi(s) = \frac{\varphi_m}{L}\,s, \tag{7}$$

which can accurately approximate the deformed shape of the specimen for moderate bending and twisting angles. The corresponding expression of $\widehat{E}_{tot}(\theta_0, \vartheta_m, \varphi_m)$ obtained after substituting (7) into (2) is given in the appendix.

Note that the model (A.1) being nonlinear, only numerical solutions can be derived. However, a great deal of insight into the specimen behaviour can still be gained by taking a fourth order expansion with respect to ϑ_m and φ_m, i.e.,

$$\widehat{E}_{tot}(\theta_0, \vartheta_m, \varphi_m) = \widetilde{E}_{tot}(\theta_0, \vartheta_m, \varphi_m) + \mathrm{O}(\{\vartheta_m, \varphi_m\}^5), \tag{8}$$

and studying the approximate energy $\widetilde{E}_{tot}$, which is a fourth order polynomial of the mechanical descriptors ϑ_m and φ_m and hence can have up to three minima. The undeformed configuration, i.e., $\varphi_m = 0$ and $\vartheta_m = 0$, is a local minimum of $\widetilde{E}_{tot}$ (and of $\widehat{E}_{tot}$) whose stability can be studied by analysing

the corresponding Hessian matrix

$$\boldsymbol{H}(\theta_0) = \left[\begin{array}{cc} \dfrac{\partial^2 \widetilde{E}_{tot}}{\partial \vartheta_m^2} & \dfrac{\partial^2 \widetilde{E}_{tot}}{\partial \vartheta_m \partial \varphi_m} \\ \dfrac{\partial^2 \widetilde{E}_{tot}}{\partial \vartheta_m \partial \varphi_m} & \dfrac{\partial^2 \widetilde{E}_{tot}}{\partial \varphi_m^2} \end{array} \right]_{\vartheta_m=0, \varphi_m=0} . \tag{9}$$

From this, it is seen that up to the critical value $B_y^{(crit)}$ of the magnetic field

$$B_y^{(crit)} = \sqrt{\frac{3\ \mathrm{EI}}{L^4\, \chi \left(\mathrm{EI}/\mathrm{GJ} \sin^2(\theta_0) + \cos^2(\theta_0) \right)}}\,, \tag{10}$$

the undeformed configuration is a stable equilibrium position (the determinant of the Hessian matrix is strictly positive). As soon as $B_y \geq B_y^{(crit)}$ the configuration becomes unstable (local maximum of the energy) and two other symmetric minima appear. The presence of two symmetric minima is due to the fact that positive or negative bending/twisting angles have the same weights in the energy. In this situation the reinforcing fibres attempt to align to the magnetic field lines, and for a given specimen there is a magnetic field strength, $B_y^{(crit)}$, at which a sudden increase in actuation angle is observed (See Fig. 10).

The value of $B_y^{(crit)}$ can be experimentally determined by slowly increasing the intensity of the magnetic field up to the point at which a sudden jump in the deformation of the beam is observed. This effect was experimentally observed and is shown in Fig. 10 for selected specimens with fibres at $\theta_0 =$ 15°, 45°, 75° and 90°. For example, at $\theta_0 = 75°$ this magnetic field strength, $B_y^{(crit)}$, is seen when the magnetic field overcomes ∼0.07 T and a sudden increase in the bending angle occurs. This is clearly visible from the camera samples in the figure. The experimentally determined values of $B_y^{(crit)}$ for the angles {0°, 15°, 30°, 45°, 60°, 75°, 90°} are {0.137, 0.103, 0.097, 0.080, 0.080, 0.074, 0.069} T respectively, that by fitting Eq. (10) give a value of $\chi_a = 2.20 \times 10^{-3}$. It should be noted that this value is about thirty times larger than the one reported in the literature for neat carbon fibres [16] and is likely due to the nickel functionalisation of the fibres, which make them easier to orient in low magnetic fields.

Note that the small increase in the actuation angles for values lower than the critical magnetic field intensity, $B_y^{(crit)}$, is thought to be caused by the fibres not being completely aligned and having a spread in the orientation,

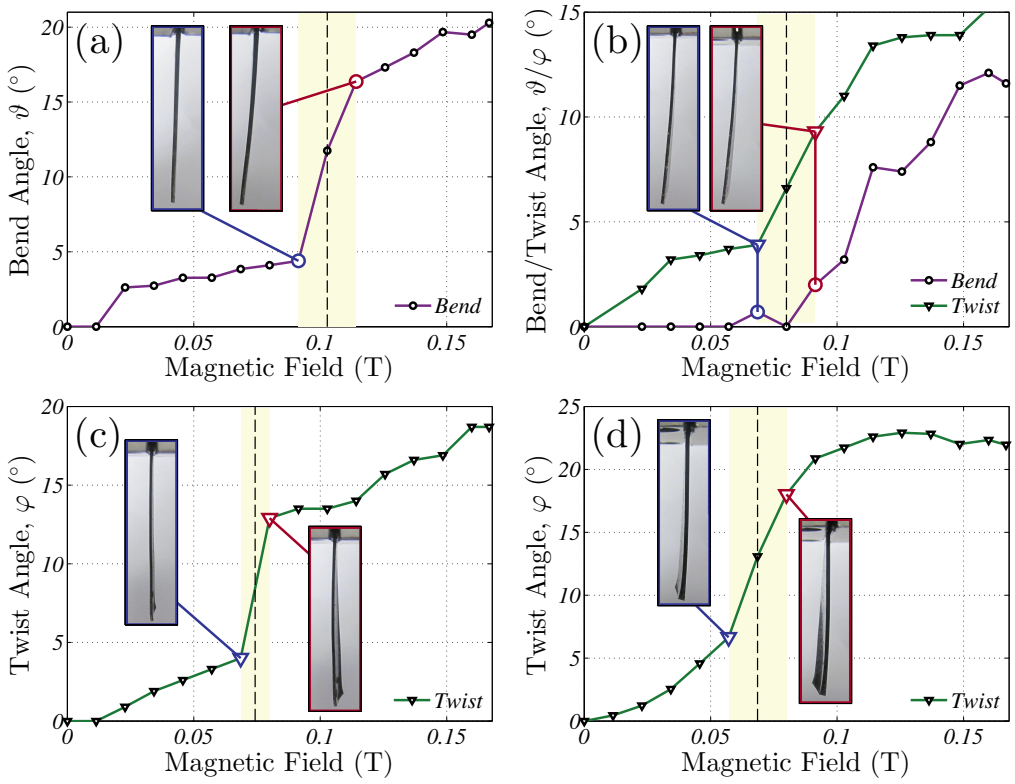

Figure 10: Bending and twisting angles, in terms of the intensity of the magnetic field, for specimens with fibres at (a) $\theta_0 = 15°$, (b) $\theta_0 = 45°$, (c) $\theta_0 = 75°$ and (d) $\theta_0 = 90°$. When the magnetic field overcomes a certain field strength ($B_y^{(crit)}$), a sudden increase in the actuation angle is observed. The insets show the pictures of the actual sample during the experiment.

as shown in Fig. 3a. It is also observed that in each case, a dominant mode of actuation angle is present that suppresses the other, as shown by the relatively low bending angle, compared to the twisting angle, for $\theta_0 = 45°$. **In the other cases, the suppressed actuation mode is too small to measure.**

The minimisation of $\widetilde{E}_{tot}$ allows the positions of each fibre orientation to be worked out as a function of the magnetic field, as shown in Fig. 12 where the mid-point of the observed stability is compared to the model prediction; this was obtained with the parameters calculated in Fig. 11. At 0° the specimen exhibits bending only, whereas at 90° only twisting is ob-

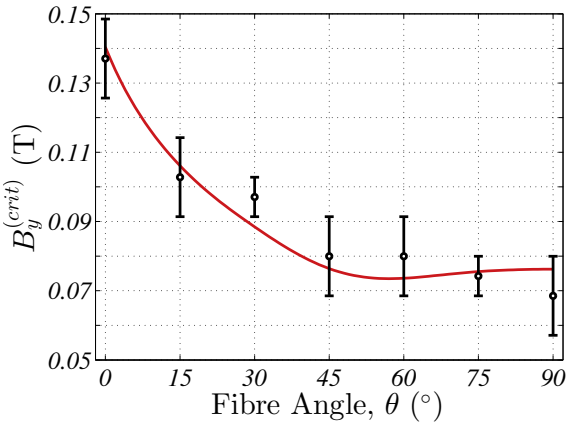

Figure 11: Critical magnetic field intensity $B_y^{(crit)}$ at which the undeformed configuration becomes unstable, assuming the model (10). (Parameters: E(θ_0) and G(θ_0) taken from the results of the mechanical testing, I = 1.26×10^{-13} (m^4), J = 4.77×10^{-13} (m^4), L = 27.5×10^{-3} (m), $\chi_a = 2.20\times10^{-3}$ and $\nu_f = 6$ %). The black dots represent the results of the experiment carried out by the authors for specimens with fibres at $\theta_0 = \{0°, 15°, 30°, 45°, 60°, 75°, 90°\}$.

served. Fibre angles in between show both bending and twisting. The results of the experiments are shown in the same figure with orange dots representing the bending angles of specimens with $\theta_0 = \{0°, 15°, 30°, 90°\}$. The corresponding twisting angles are shown with purple dots for specimens with $\theta_0 = \{0°, 45°, 60°, 75°, 90°\}$.

Although a certain degree of dispersion in the fibre angle is present (see the distribution function in Fig. 3), the actuation of the specimens in the magnetic field confirm the behaviour predicted by the model. Indeed, as seen in Fig. 13, a 0° specimen exhibited only bending, whilst only twisting is observed at 90°. At angles between, either twisting or bending is observed as the dominant actuation mechanism; although it is still possible to observe both (see Fig. 13b).

4. Conclusions

In this study, thin film samples of a novel NiC-PDMS composite were fabricated using low magnetic fields to orientate the fibres and create transversely isotropic samples. The fibres were dispersed in the host matrix using sonication and mechanical mixing. It was observed that successful dispersion

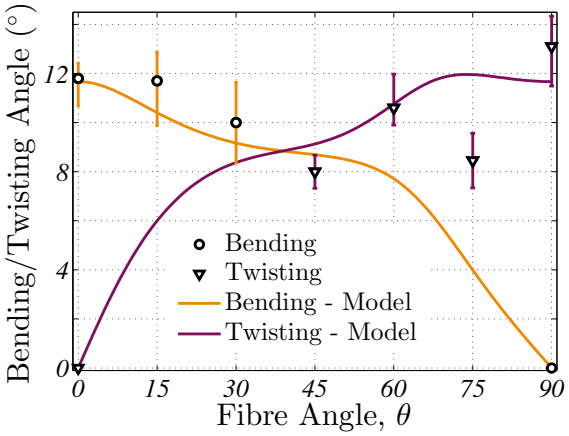

Figure 12: Bending and twisting angles achieved for an imposed orthogonal magnetic field at the occurrence of the instability. The actuation angle at the mid-point of the instability is indicated, with the error bars indicating the range of the actuation angle within the mid-25% of the instability magnetic field range highlighted in Fig. 10. (Parameters: $E(\theta_0)$ and $G(\theta_0)$ taken from the results of the mechanical testing, I = 1.26×10^{-13} (m^4), J = 4.77×10^{-13} (m^4), L = 27.5×10^{-3} (m), $\chi_a = 2.20\times10^{-3}$ and $\nu_f = 6$ %). The orange and purple dots represent respectively the bending and twisting results of the experiment carried out by the authors for specimens with fibres at $\theta_0 = \{0°, 15°, 30°, 45°, 60°, 75°, 90°\}$.

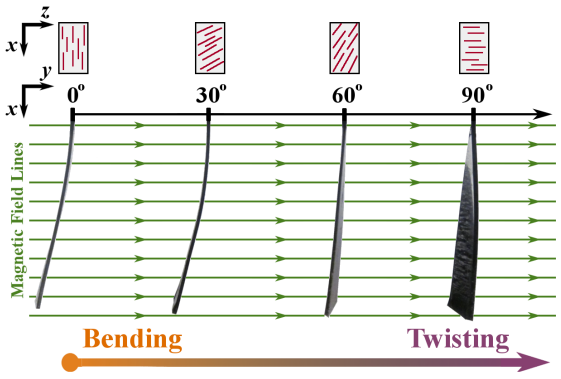

Figure 13: Static Actuation of selected specimens in a homogeneous magnetic field for 0°, 30°, 60° and 90° fibre angles (The image shows actual pictures of the specimens during tests). Specimens of length ∼27.5mm, width 7mm and thickness 0.6mm. A transition from pure bending for 0° to pure twisting for 90° is observed. For the orientation of the axes see Fig. 9

and alignment was achieved for all fibre orientations, although a small number of agglomerations and misaligned particles were evident. The presence of unaligned fibres was caused by the fibres having lost their Nickel coating, as confirmed by SEM images. The resulting materials had mechanical properties that were controlled by the strength and direction of the magnetic field during the curing phase.

This novel composite was actuated magnetically to determine its potential for use in micro-actuator systems. Thanks to the nickel functionalisation of the fibres, a low magnetic field was used (< 0.2 T). The average anisotropic susceptibility of the fibres identified from the experiments was $\chi_a = 2.20 \times 10^{-3}$, which is about thirty times larger than the one reported in the literature for neat carbon fibres and suggests the beneficial effect of the nickel coating on the magnetic properties. The composite actuator has a large displacement capability, with a multistable behaviour induced by the magnetic torque acting on the fibres: the samples remained undeformed up to a critical value of the magnetic field after which a sudden increase in the deformation occurred. Both twisting and bending behaviour was independently observed at different initial orientations of the fibre and predicted by the simple model introduced. By controlling the orientation of the external magnetic field, the combination of bending and twisting in the actuators could be utilised to develop complex steering mechanisms for use in a wide variety of micro-actuator systems such as micro-pumps and micro-valves.

Future work would now require the testing of this material in low Reynolds number flow and if this is successful, development of a device and further testing would be required to determine the potential propulsive speeds of this system. The propulsive force and speed can then be used to determine if such a system is comparable to existing micro-swimming devices[10]. **Initial work presented in the supplementary materials has indicated that the strain rate dependence of the material is limited, and that the presented model could be adapted to model a micro-actuating device at moderate speeds. In addition, cyclic deformation shows minimal plastic deformation, encouraging its use as a large strain actuating device. However,** envisaging the material for larger strain applications would also require improvements to the fibre-matrix interface.

Acknowledgements

This work was supported by the Engineering and Physical Sciences Research Council through the EPSRC Centre for Doctoral Training in Advanced Composites for Innovation and Science [grant number EP/G036772/1]. The authors wish to thank Mr. G. L. Thompson and Miss. L. Edwards for support in the experiments.

[1] Brigadnov, I. & A. Dorfmann (2003). Mathematical modeling of magneto-sensitive elastomers. *International Journal of Solids and Structures 40*(18), 4659–4674.

[2] Camponeschi, E., R. Vance, M. Al-Haik, H. Garmestani, & R. Tannenbaum (2007). Properties of carbon nanotube-polymer composites aligned in a magnetic field. *Carbon 45*(10), 2037–2046.

[3] Choi, E. S., J. S. Brooks, D. L. Eaton, M. S. Al-Haik, M. Y. Hussaini, H. Garmestani, D. Li, & K. Dahmen (2003). Enhancement of thermal and electrical properties of carbon nanotube polymer composites by magnetic field processing. *Journal of Applied Physics 94*(9), 6034.

[4] Ciambella, J. & D. Stanier (2014). Orientation Effects in Short Fibre-Reinforced Elastomers. In *Proceedings of ASME 2014 International Mechanical Engineering Congress and Exposition*, Montreal. American Society of Mechanical Engineers (ASME).

[5] Curley, R., M. Fisher, D. J. V, W. Marsh, S. Assigned, & M. Corporation (1996). Rubber composites, in particular vehicle tires, having a three dimensional reinforcement structure. Patent 5447776.

[6] Curtis, J. & A. Colas (2004). Medical applications of silicones. *Biomaterials science: an introduction to materials in medicine*, 697–707.

[7] Erb, R. M., R. Libanori, N. Rothfuchs, & A. R. Studart (2012). Composites reinforced in three dimensions by using low magnetic fields. *Science (New York, N.Y.) 335*(6065), 199–204.

[8] Feher, J., G. Filipcsei, J. Szalma, & M. Zrínyi (2001). Bending deformation of neutral polymer gels induced by electric fields. *Colloids and Surfaces A: Physicochemical and Engineering Aspects 183-185*, 505–515.

[9] Galipeau, E., S. Rudykh, G. DeBottom, & P. Ponte Castañeda (2014). Magnetoactive elastomers with periodic and random microstructures. *International Journal of Solids and Structures 51*, 3012–3024.

[10] Gao, W., X. Feng, A. Pei, C. R. Kane, R. Tam, C. Hennessy, & J. Wang (2014). Bioinspired helical microswimmers based on vascular plants. *Nano letters 14*(1), 305–10.

[11] Giddings, P., C. Bowen, R. Butler, & H. Kim (2008, apr). Characterisation of actuation properties of piezoelectric bi-stable carbon-fibre laminates. *Composites Part A: Applied Science and Manufacturing 39*(4), 697–703.

[12] Jeon, J.-H., S.-W. Yeom, & I.-K. Oh (2008, apr). Fabrication and actuation of ionic polymer metal composites patterned by combining electroplating with electroless plating. *Composites Part A: Applied Science and Manufacturing 39*(4), 588–596.

[13] JianFeng, Y. & S. Cho (2014). Mini and Micro Propulsion for Medical Swimmers. *Micromachines 5*(1), 97–113.

[14] Keaveny, E. E., S. W. Walker, & M. J. Shelley (2013). Optimization of chiral structures for microscale propulsion. *Nano Lett. 13*(2), 531–7.

[15] Kim, I., A. Tannanbaum, & R. Tannenbaum (2012). Anisotropic conductivity of magnetic carbon nanotubes embedded in epoxy matrices. *Carbon 49*(1), 54–61.

[16] Kimura, T., Y. Umehara, & F. Kimura (2010). Fabrication of a short carbon fiber/gel composite that responds to a magnetic field. *Carbon 48*(14), 4015–4018.

[17] Kimura, T., Y. Umehara, & F. Kimura (2012). Magnetic field responsive silicone elastomer loaded with short steel wires having orientation distribution. *Soft Matter 8*(23), 6206.

[18] Kitamura, N., K. Fukumi, K. Takahashi, I. Mogi, S. Awaji, & K. Watanabe (2011). Orientation of Carbon Nano-fiber in Carbon/Silica Composite Prepared under High Magnetic Field. *IOP Conference Series: Materials Science and Engineering 18*(5), 052008.

[19] Leng, J., L. Liu, Y. Liu, K. Yu, & S. Sun (2009). Electromechanical stability of dielectric elastomer. *Applied Physics Letters 94*(21).

[20] Liu, L., Y. Liu, Z. Zhang, B. Li, & J. Leng (2010). Electromechanical Stability of Electro-Active Silicone Filled with High Permittivity Particles Undergoing Large Deformation. *Smart Materials and Structures 19*(11).

[21] Liu, Y., L. Liu, Z. Zhang, Y. Jiao, S. Sun, & J. Leng (2010). Analysis and Manufacture of an Energy Harvester based on a Mooney-Rivlintype Dielectric Elastomer. *(EPL) Europhysics Letters 90*(3).

[22] Liu, Y., L. Liu, Z. Zhang, & J. Leng (2009). Dielectric Elastomer Film Actuators: Characterization, Experiment and Analysis. *Smart Materials and Structures 18*(9), 1–10.

[23] Martin, C., J. Sandler, A. Windle, M.-K. Schwarz, W. Bauhofer, K. Schulte, & M. Shaffer (2005). Electric field-induced aligned multi-wall carbon nanotube networks in epoxy composites. *Polymer 46*(3), 877–886.

[24] Martin, J. E. (2005, apr). Using triaxial magnetic fields to create optimal particle composites. *Composites Part A: Applied Science and Manufacturing 36*(4), 545–548.

[25] Masoud, H., B. I. Bingham, & A. Alexeev (2012). Designing maneuverable micro-swimmers actuated by responsive gel. *Soft Matter 8*(34), 8944.

[26] Meeker, D. C. (2006). Finite Element Method Magnetics, Version 4.0.1.

[27] Meng, Q. & J. Hu (2009, nov). A review of shape memory polymer composites and blends. *Composites Part A: Applied Science and Manufacturing 40*(11), 1661–1672.

[28] Prolongo, S., B. Meliton, G. Del Rosario, & A. Ureña (2013). New alignment procedure of magnetite-CNT hybrid nanofillers on epoxy bulk resin with permanent magnets. *Composites Part B: Engineering 46*, 166–172.

[29] Rikken, R. S. M., R. J. M. Nolte, J. C. Maan, J. C. M. van Hest, D. a. Wilson, & P. C. M. Christianen (2014). Manipulation of micro- and nanostructure motion with magnetic fields. *Soft matter 10*(9), 1295–308.

[30] Rudykh, S. & K. Bertoldi (2013). Stability of anisotropic magnetorheological elastomers in finite deformations: A micromechanical approach. *Journal of the Mechanics and Physics of Solids 61*(4), 949–967.

[31] Rudykh, S., A. Lewinstein, G. Uner, & G. DeBotton (2013). Analysis of microstructural induced enhancement of electromechanical coupling in soft dielectrics. *Applied Physics Letters 102*(15), 151905.

[32] Sharma, A., B. Tripathi, & Y. Vijay (2010). Dramatic Improvement in properties of magnetically aligned CNT/polymer nanocomposites. *Journal of Membrane Science 361*(1-2), 89–95.

[33] Silva, C. A., C. Viana, F. W. J. V. Hattum, & M. Cunha (2006). Fiber Orientation in Divergent / Convergent Flows in Expansion and Compression Injection Molding. *Polymer Composites 27*(5), 539–551.

[34] Stanier, D., A. J. Patil, C. Sriwong, S. S. Rahatekar, & J. Ciambella (2014). The Reinforcement Effect of Exfoliated Graphene Oxide Nanoplatelets on the Mechanical and Viscoelastic Properties of Natural Rubber. *Composites Science and Technology 95*, 59–66.

[35] Takeyama, S., S. Nakamura, & K. Uchida (2006). Dynamical orientation of carbon nanotubes by pulsed magnetic fields. *J. Phys. Conf. Ser. 51*, 446–449.

[36] Taya, M. (1999). Micromechanics modeling of smart composites. *Composites Part A: Applied Science and Manufacturing 30*(4), 531–536.

[37] Tipton, C. R., E. Han, & T. Mullin (2012). Magneto-elastic buckling of a soft cellular solid. *Soft Matter 8*(26), 6880–6883.

[38] Varga, Z., G. Filipcsei, & M. Zrínyi (2005). Smart composites with controlled anisotropy. *Polymer 46*(18), 7779–7787.

[39] Varga, Z., G. Filipcsei, & M. Zrínyi (2006). Magnetic field sensitive functional elastomers with tuneable elastic modulus. *Polymer 47*(1), 227–233.

[40] Zrinyi, M., L. Barsi, D. Szabo, & H.-G. Kilian (1997). Direct observation of abrupt shape transition in ferrogels induced by nonuniform magnetic field. *The Journal of Chemical Physics 106*(13), 5685.

Appendix A. Appendix

Appendix A.1. Total Energy of the Magnetic Beam

By substituting (7) into (2) one obtains the following expression of the total energy of the beam in terms of the mechanical descriptors ϑ_m, φ_m and the fibre orientation in the undeformed configuration θ_0

$$\begin{aligned}\widetilde{E}_{tot} &= \frac{\mathrm{EI}}{2L^3}\vartheta_m^2 + \frac{\mathrm{GJ}}{2L^3}\varphi_m^2 - \frac{B_y^2 L\chi\cos(\theta_0)^2}{8\vartheta_m}(2\vartheta_m - \sin(2\vartheta_m)) + \\ &+ \frac{B_y^2 L\chi\sin(2\theta_0)}{8\vartheta_m}(\varphi_m\cos(\varphi_m)\sin(2\vartheta_m) - 2\vartheta_m\cos(2\vartheta_m)\sin(\varphi_m)) + \\ &- \frac{1}{32}B_y^2 L\chi\sin(\theta_0)^2 \\ &\left(4 + \frac{2\sin(2\vartheta_m)}{\vartheta_m} - \frac{\sin(2(\vartheta_m-\varphi_m))}{\vartheta_m-\varphi_m} - \frac{2\sin(2\varphi_m)}{\varphi_m} - \frac{\sin(2(\vartheta_m+\varphi_m))}{\vartheta_m+\varphi_m}\right)\end{aligned} \tag{A.1}$$

In the derivation of (A.1), the magnetic field is assumed to be directed along the y-axis only, i.e., $\boldsymbol{B} = \{0, B_y, 0\}$ as per in the experimental setup used.

Appendix B. Supplementary Material

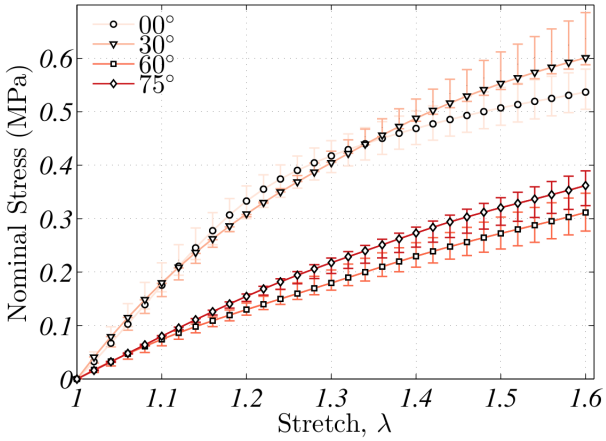

Figure B.14: Nominal stress (engineering stress) vs stretch ($\lambda = l/l_0$), showing confidence intervals of 90% derived from the stress-strain data at angles 0°, 30°, 60° and 75°.

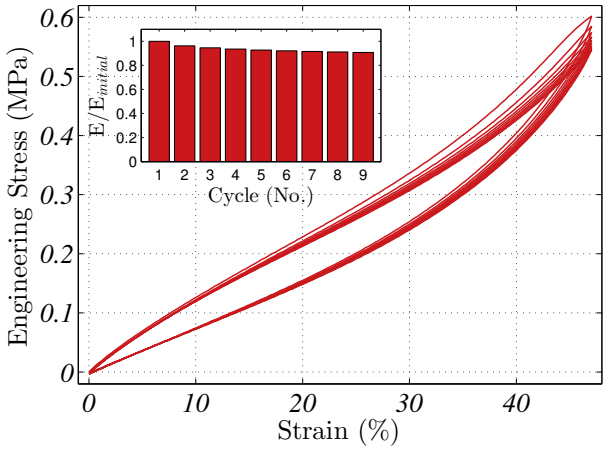

Figure B.15: Cyclic mechanical testing of a PDMS sample reinforced with fibres aligned at 0°.Testing to 60% strain is shown for 10 cycles without a magnetic field, after 3 initial cycles to condition the specimen. Inset: The normalised small strain modulus at the beginning of each cycle.

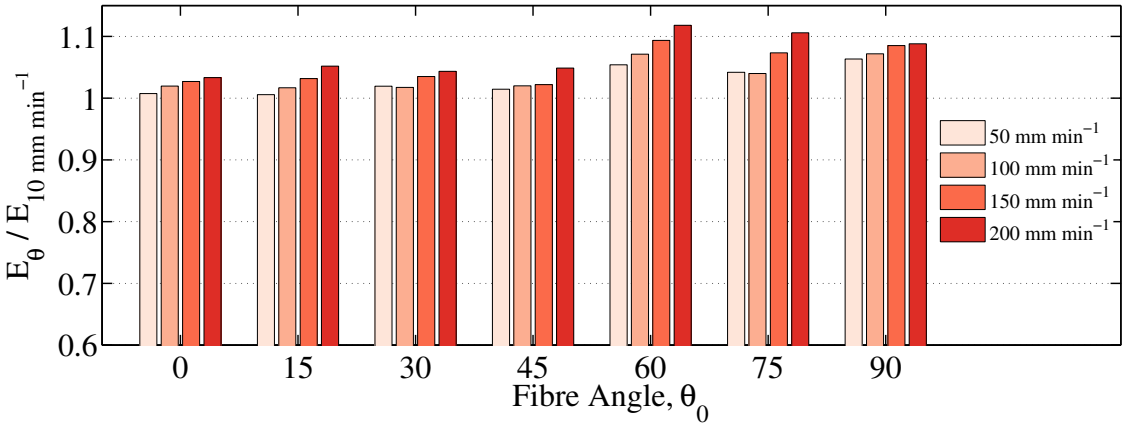

Figure B.16: Mechanical testing of the specimens at different strain rates, normalised against the quasi-static results. Loading rates of 10 (quasi-static), 50, 100, 150 and 200 mm min-1 (strain rates of 1.36x10^{-2}, 6.80x10^{-2}, 1.36x10^{-1}, 2.04x10^{-1} and 2.72x10$^{-1}s^{-1}$ respectively).

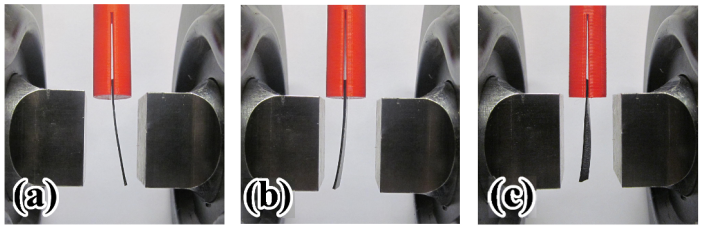

Figure B.17: Actuation mechanisms of selected specimens within the platelet of the electromagnet used to generate a homogeneous magnetic field, (a) 0°, (b) 45°, (c) 90°. Specimens of length 25mm, width 7mm and thickness 1mm.

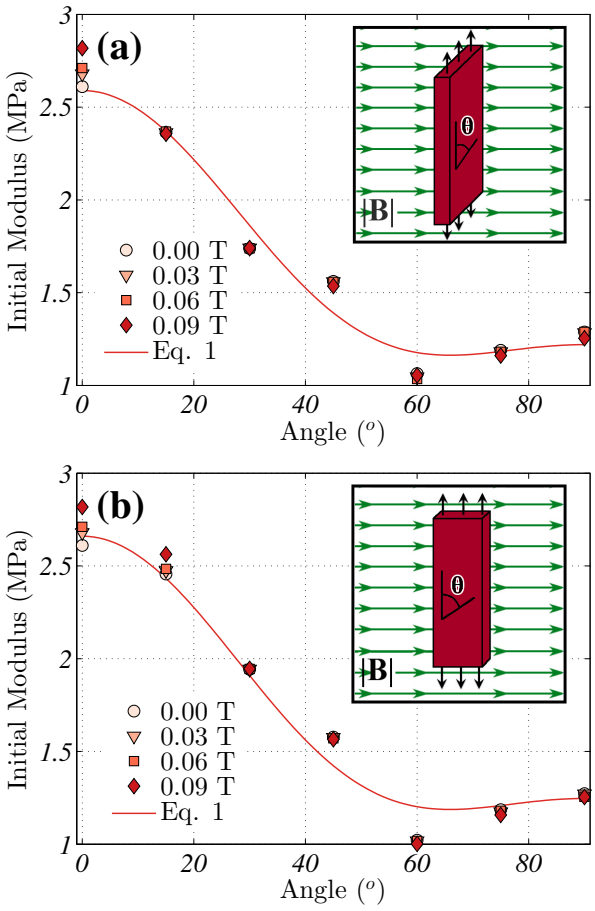

Figure B.18: The small strain modulus of aligned, nickel-coated carbon fibre reinforced PDMS samples oriented in two configurations: (a) The specimen thickness parallel to the magnetic field, (b) The specimen width parallel to the magnetic field. Tested at reinforcement angles of 15° intervals between 0° and 90°, and at four magnetic field strengths.